Schweizerischer Erdbebendienst
Service Sismologique Suisse
Servizio Sismico Svizzero
Swiss Seismological Service

ETH zürich

SITE CHARACTERIZATION REPORT

SIZS: Ilanz/Glion (GR) - Schule

Manuel Hobiger, Donat Fäh

Last Modification: 25/02/2020

Schweizerischer Erdbebendienst (SED)
Service Sismologique Suisse
Servizio Sismico Svizzero
Servizi da Terratrembels Svizzer

ETH Zürich
Sonneggstrasse 5
8092 Zürich
Schweiz
manuel.hobiger@sed.ethz.ch

Contents

Summary

The free-field strong-motion station SIZS was built next to the school in Ilanz/Glion (GR). We performed a passive seismic array measurement to characterize the soil underneath the station.
The measurements show that the structure beneath the station has a first, wide fundamental frequency peak at around 1 Hz and a second, more pronounced peak at 4 Hz. The array measurements were analyzed with different techniques, namely 3-component high-resolution FK (HRFK), WaveDec and Spatial Autocorrelation (SPAC). All techniques gave similar dispersion curves. The dispersion curves for the fundamental modes of both Love and Rayleigh waves could be retrieved from around 2.1 to 42 Hz and 2.6 to 29.7 Hz, respectively.
The joint inversion of Love and Rayleigh wave dispersion curves and the Rayleigh wave ellipticity angle showed that the structure can be explained by models with interfaces at about 10 m and 40 m depth. The V_{S30} of the best models is about 423 m/s, corresponding to soil class B in EC8 and C in SIA261.

1 Introduction

In the framework of the second phase of the Swiss Strong Motion Network (SSMNet) renewal project, a new station was planned in Ilanz/Glion (GR).
The station is located close to the school. The new station, called SIZS, went operational on 25 May 2016. The location of the station is shown in Fig. 1.

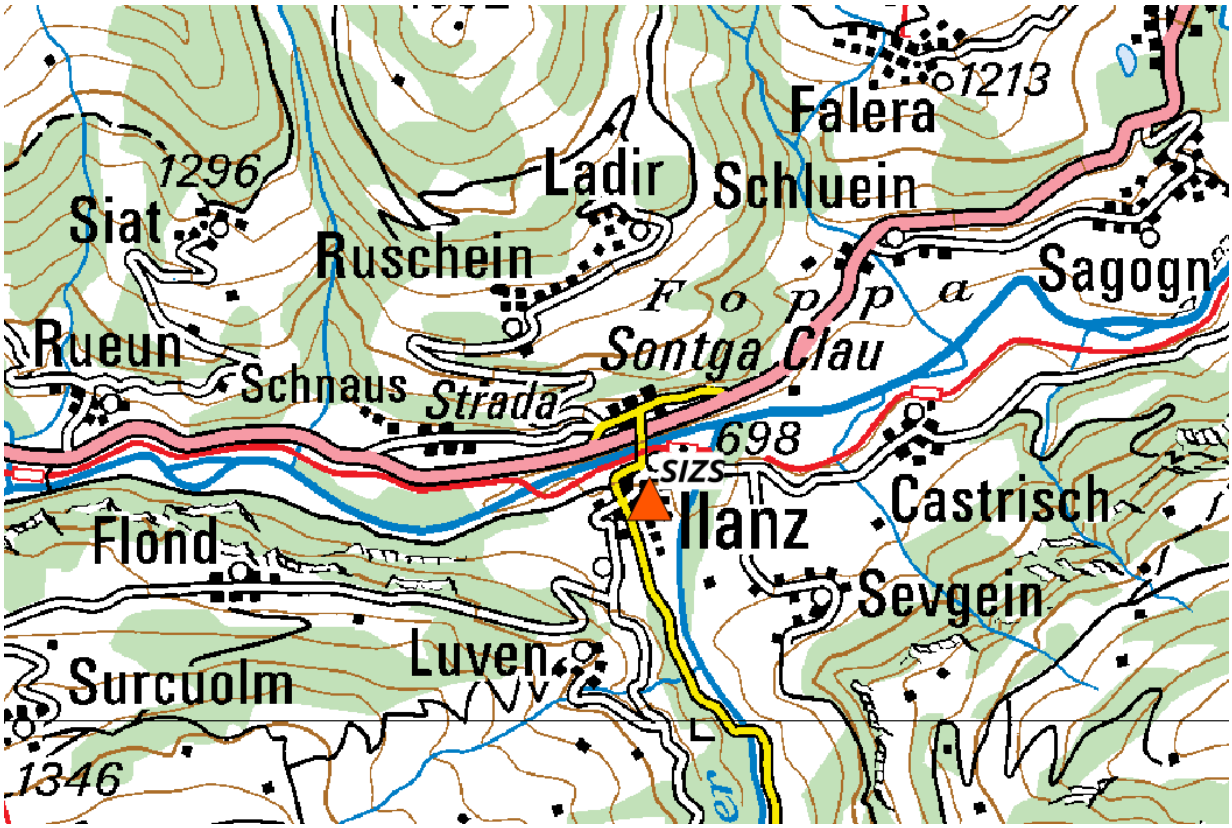

Figure 1: Map showing the location of station SIZS in Ilanz. ©2019 swisstopo (JD100042)

2 Geological setting

A geological map of the surroundings of station SIZS is shown in Fig. 2. The station is located on moraine. Further east, alluvial deposits are found.

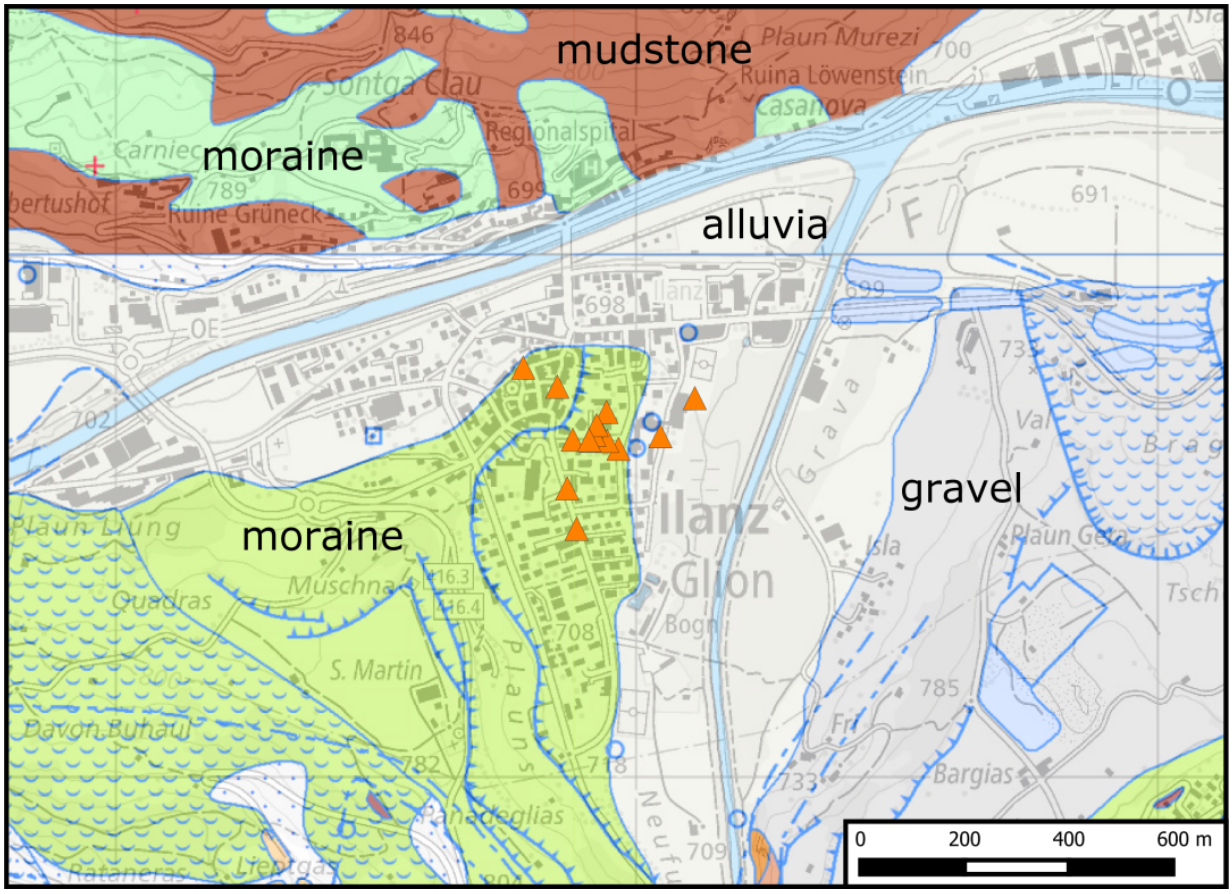

Figure 2: Geological map of the area around station SIZS with the different stations of the array measurement (orange triangles). Station SIZS is located in the center of the array. According to the geological atlas, station SIZS and most stations of the passive array measurement lie on moraine, some stations to the east lie on alluvial deposits. ©2019 swisstopo (JD100042)

3 Site characterization measurements

3.1 Data set

In order to characterize the local underground structure around station SIZS, a passive seismic array measurement was carried out on 8 October 2016. The layout of the seismic measurements is shown in Fig. 3.
A single array measurement was performed. The array consisted of 16 stations. It was planned to consist of five rings of three stations each around a central station, which was located close to station SIZS. The ring radii were planned to be 8 m, 20 m, 48 m, 120 m, and 200 m, respectively. The final minimum and maximum inter-station distances in the array were 7.9 m and 338.2 m, respectively. The names of the stations of the array are composed of "SIZS" followed by a two-digit number (42 to 49, 52 to 55, 62, 64, 72, 73). The seismic stations consisted of Lennartz 3C 5 s sensors connected to Centaur digitizers. A total of 12 digitizers were used. Twelve sensors were connected to the A channels of the digitizers and another four sensors were connected to B channels. The total recording time was 195 minutes.
The station locations have been measured by a differential GPS system (Leica Viva GS10) which was set up to measure with a precision better than 5 cm. This precision was achieved for all stations except SIZS55. This station, located to the northeast, was shadowed by high buildings. There, the precision of the measurement was only 88.8 cm.

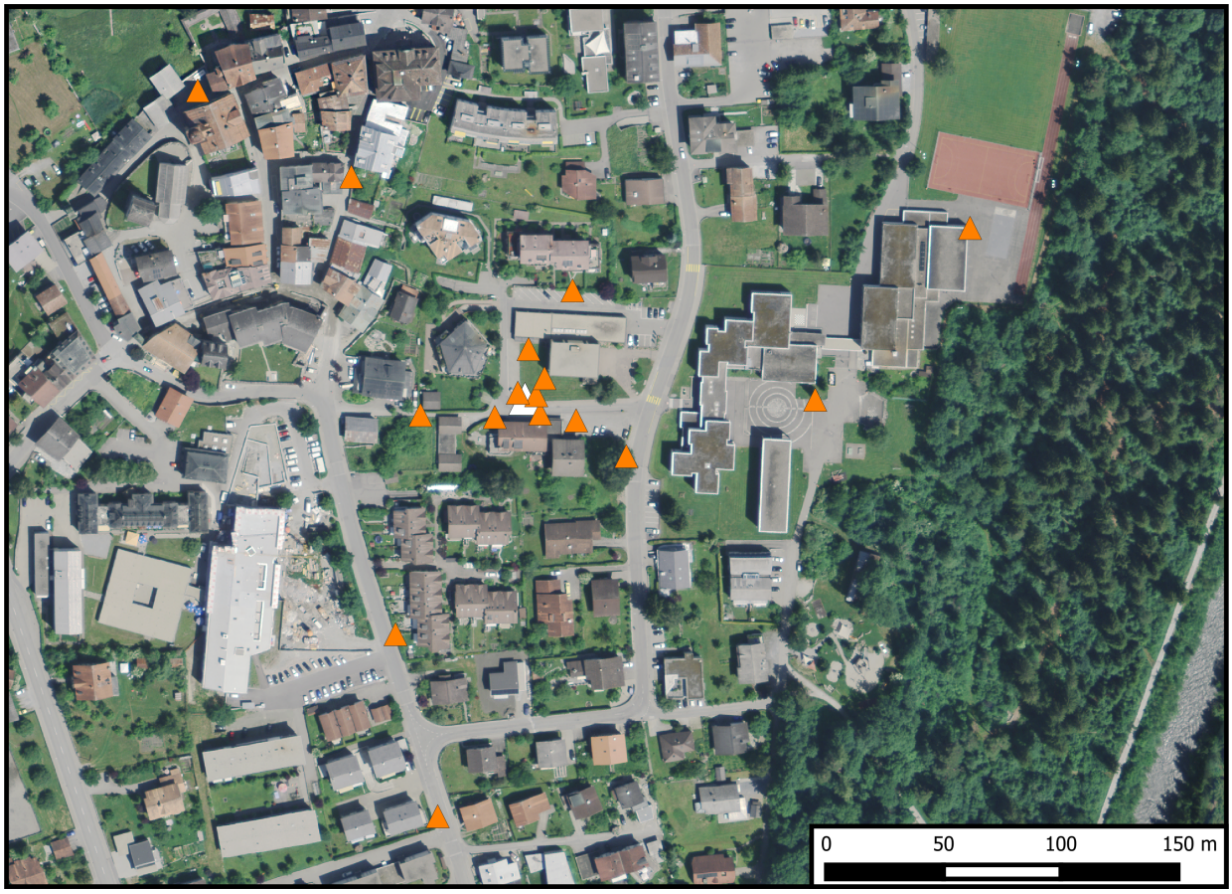

Figure 3: Layout of the array measurements around station SIZS. The location of SIZS is indicated by the white triangle, the locations of the stations for the passive seismic measurement by the orange triangles. ©2019 swisstopo (JD100042)

3.2 H/V and RayDec ellipticity curves

Figure 4 shows the H/V curves determined with the time-frequency analysis method (Fäh et al., 2009) for all stations of the passive array. All curves are rather similar and show two major peaks. The first one is a plateau located between 0.7 and 2 Hz. The second peak is more pronounced and ranges from 3.35 and 5.68 Hz for the different stations. We can observe some variations between the different stations. The curves of the center of the array were the most similar ones. For station SIZS44, located close to the permanent station SIZS, this peak was picked at 4.22 Hz.
The RayDec technique (Hobiger et al., 2009) is supposed to eliminate the contributions of other wave types than Rayleigh waves and give a better estimate of the ellipticity than the classical H/V technique. The RayDec ellipticity curves for all stations of the array measurement are shown in Fig. 4 and are similar to the H/V curves. Station SIZS44, the central station of the array, serves as a reference and will be used for the inversion.

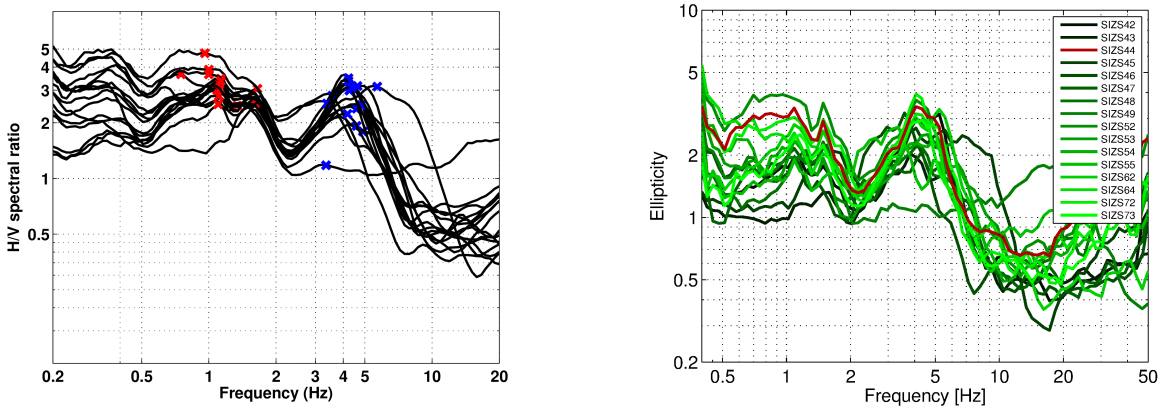

Figure 4: Left: Overview of the H/V measurements for the different stations of the array measurements. Right: RayDec ellipticities for all measurement stations. The red curve corresponds to SIZS44, the central station of the array.

3.3 Polarization measurements

The polarization analysis was performed according to Burjánek et al. (2010) and Burjánek et al. (2012). The results for all stations of the array are similar. Only the results for SIZS44, the station in the array center, are shown here.
There is no preferential linear particle polarization visible and we do not see indications for 2-dimensional polarization effects.

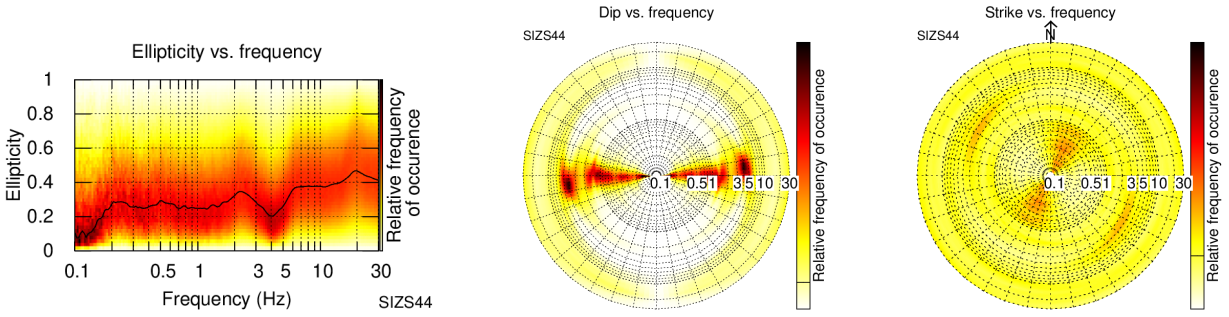

Figure 5: Polarization analysis of station SIZS44.

3.4 3-component high-resolution FK

The results of the 3-component high-resolution FK analysis (Poggi and Fäh, 2010) are shown in Fig. 6. On the transverse component, corresponding to Love waves, we can clearly identify a dispersion curve between 2.1 and 42.0 Hz, spanning the complete accessible frequency range between the array resolution limits. A second mode is visible between 8.2 and 11.0 Hz.
On the vertical component, corresponding to Rayleigh waves, we can clearly identify one mode between 2.6 and 29.7 Hz, also spanning the complete range of accessible frequencies. On the radial component, also related with Rayleigh waves, the results are less clear, but we can also see the dispersion curve between 2.6 and 28.3 Hz.
The corresponding ellipticity curves of these modes show two weak peaks at around 4 Hz and 14 Hz.

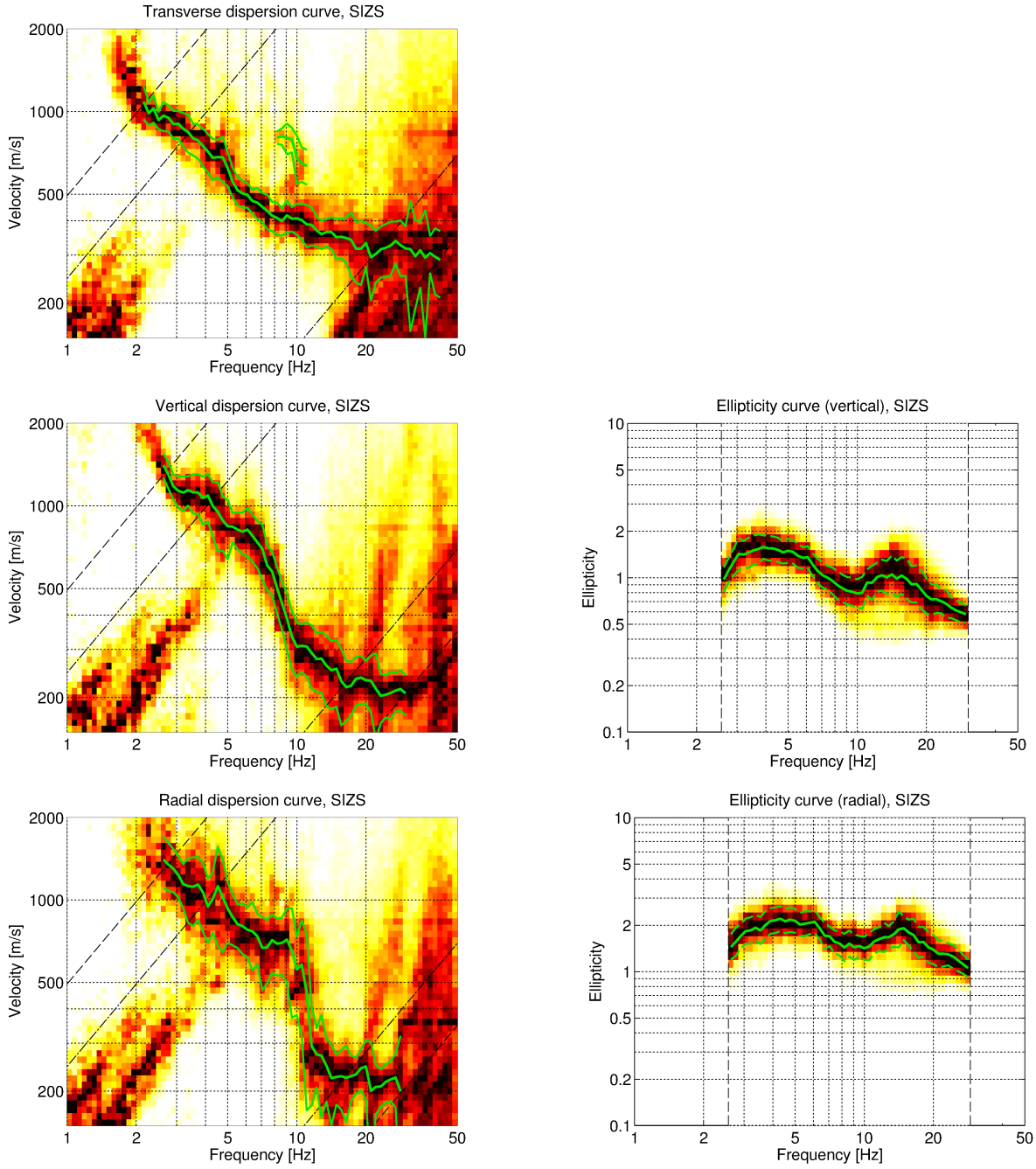

Figure 6: Dispersion and ellipticity curves obtained with the 3-component HRFK algorithm (Poggi and Fäh, 2010). In the left column, the dispersion curves for the transverse, vertical and radial components are shown, and in the right column the ellipticity curves corresponding to the dispersion curves picked on the vertical and radial components. The dashed and dotted black lines are the array resolution limits. The solid green lines are picked from the data, where the central line indicates the best values and the two outer lines the standard deviation.

3.5 WaveDec

The results of the WaveDec (Maranò et al., 2012) processing are shown in Fig. 7. This technique estimates the properties of single or multiple waves simultaneously with a maximum likelihood approach. In order to improve the results, the parameter γ, which modifies the sharpness of the wave property estimation, has been tuned. Here, a value of $\gamma = 0.2$ was used, corresponding to a predominantly maximum likelihood estimation. The Love wave dispersion curve is clearly identified between 1.9 and 15.7 Hz, without reaching the upper-frequency theoretical array resolution limit. However, the picking is less clear than for HRFK.
The Rayleigh wave dispersion curve is retrieved between 2.5 and 25.4 Hz and, similarly to the Love wave curve, not as clear as the HRFK curve. The ellipticity angle for the picked Rayleigh wave dispersion curve is negative below 3.5 Hz, corresponding to retrograde particle motion, and positive from 3.7 to 9.0 Hz, corresponding to prograde particle motion. Above, we assume it to be negative, i.e. retrograde, again, but there are actually also data points with the opposite sense of rotation. this is probably due to the unclear determination of the dispersion curve.

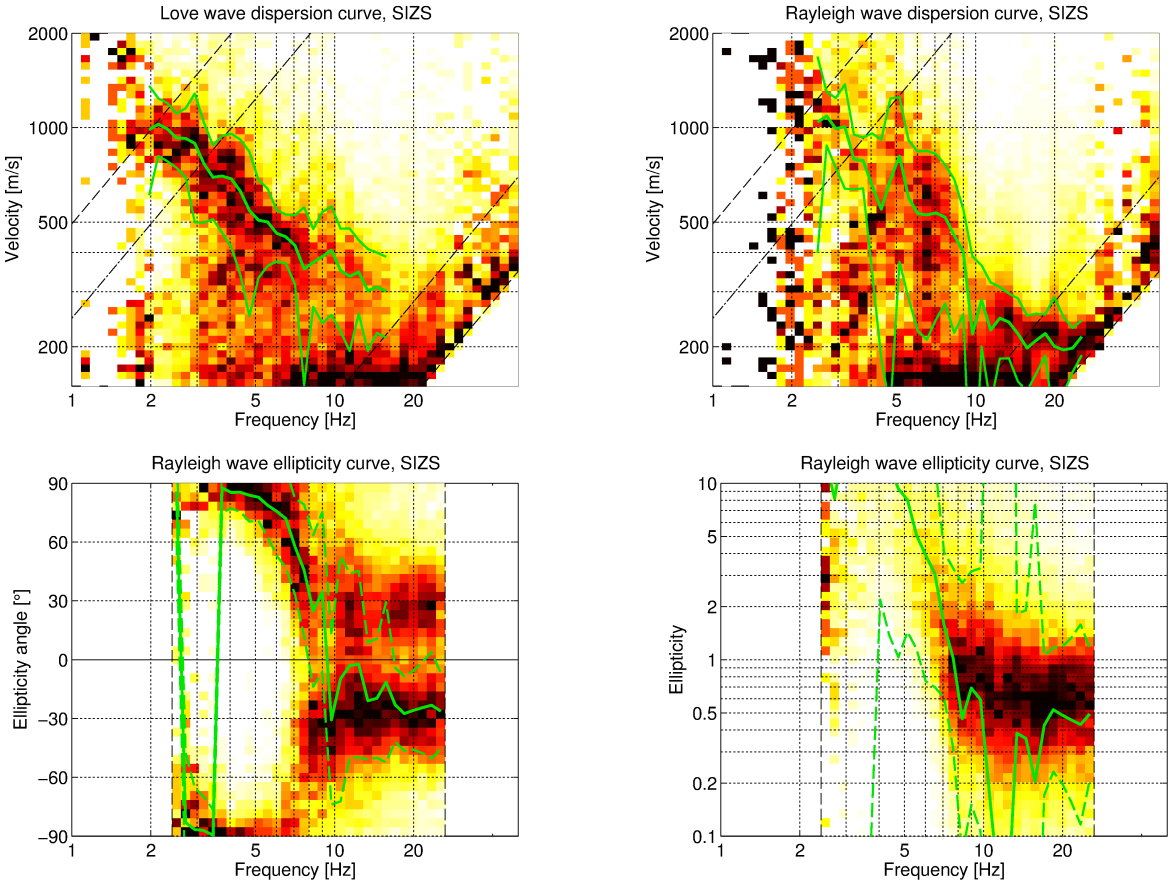

Figure 7: Top: Love (left) and Rayleigh (right) wave dispersion curves obtained with the WaveDec technique (Maranò et al., 2012). The dashed lines indicate the theoretical array resolution limits. Bottom: Rayleigh wave ellipticity angle curve for the picked dispersion curve (left) and Rayleigh wave ellipticity curve (right), i.e. the absolute value of the tangent of the ellipticity angle.

3.6 SPAC

The SPAC (Aki, 1957) curves of the vertical components have been calculated using the M-SPAC (Bettig et al., 2001) technique implemented in geopsy (Wathelet et al., 2005). Rings with different radius ranges had been defined previously and for all station pairs with distance inside this radius range, the cross-correlation was calculated over a wide frequency range. These cross-correlation curves are averaged for all station pairs of the respective ring and give the SPAC curves. The rings are defined in such a way that at least three station pairs contribute and their connecting vectors have a good directional coverage.
The SPAC curves for all defined rings are shown in Fig. 8. The black points indicate the data values which contributed to the final dispersion curve estimation, which was made with the function `spac2disp` of the geopsy package.
Using SPAC, we can retrieve a Rayleigh wave dispersion curve between 2.8 and 14.7 Hz.

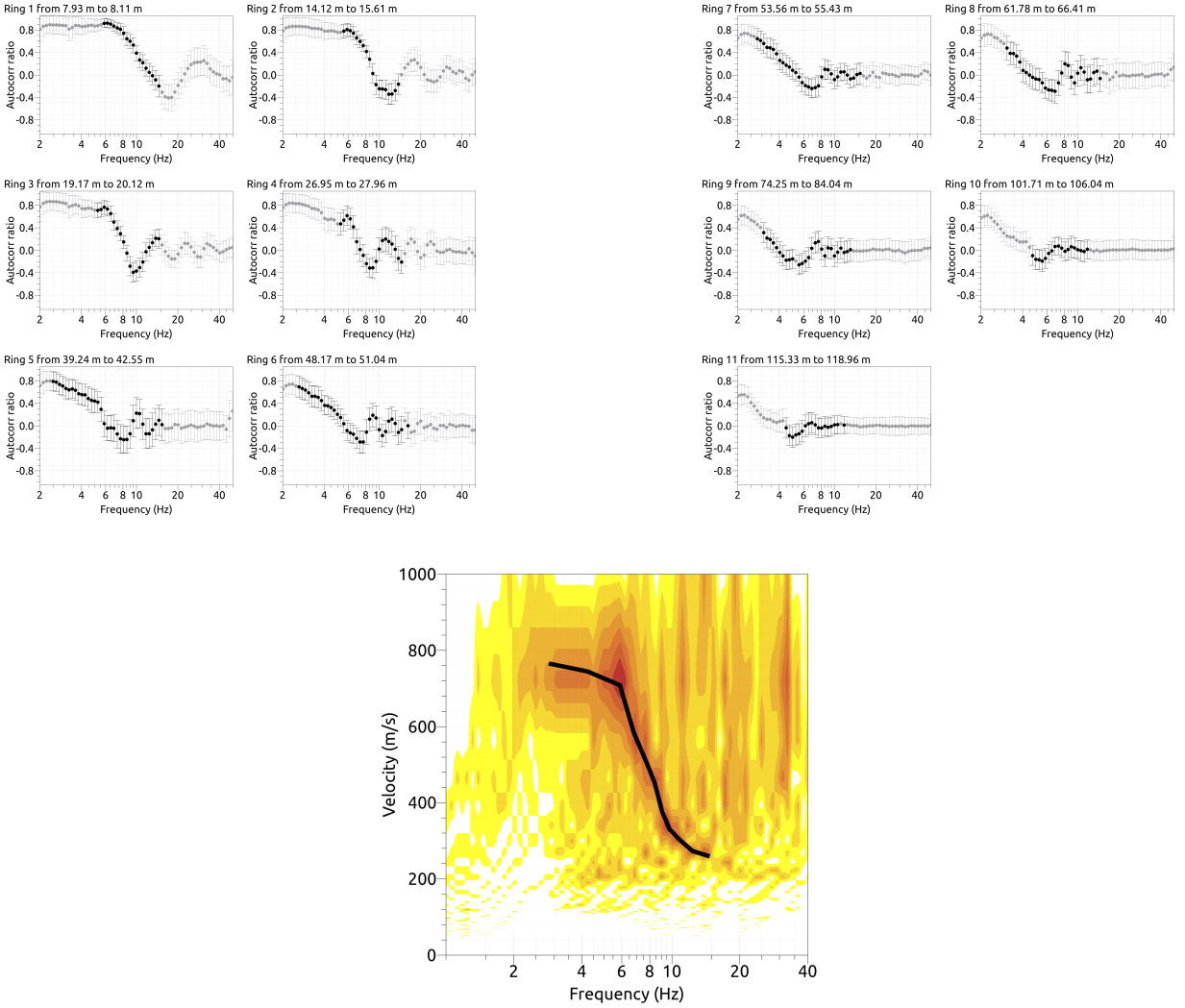

Figure 8: Top: SPAC curves for the different distance ranges. The black data points contributed to the dispersion curve estimation. Bottom: Resulting Rayleigh wave velocities. The black line corresponds to the picked dispersion curve.

3.7 Summary

Fig. 9 gives an overview of the dispersion and ellipticity curves determined by the different methods.
For Love waves, the HRFK and WaveDec results are in good agreement. The higher mode is only visible for HRFK.
For Rayleigh waves, the different methods differ more. The HRFK curves for the vertical and radial components differ at the downgoing part of the curve from 7 to 12 Hz. The SPAC curve is in good agreement with the vertical HRFK curve above 8 Hz, but shows systematically lower velocities below. The WaveDec curve is more scattered and shows lower velocities than the HRFK curves.
The ellipticity curves retrieved using the different methods are in qualitative agreement as all methods show the peaks at similar frequencies. The WaveDec ellipticity curve is more extreme than the other curves. The single-station ellipticity curve determined with RayDec also covers frequencies lower than 3 Hz. It was transformed to ellipticity angle using the arctangent function. As we cannot distinguish between prograde and retrograde particle motion with a single-station method, we account for both possibilities and the RayDec (and HRFK) curves are represented twice, once for each sense of rotation. In the ellipticity angle representation, the WaveDec curve shows retrograde particle motion below 3.8 Hz and prograde particle motion above until about 9 Hz, where it changes to retrograde again.

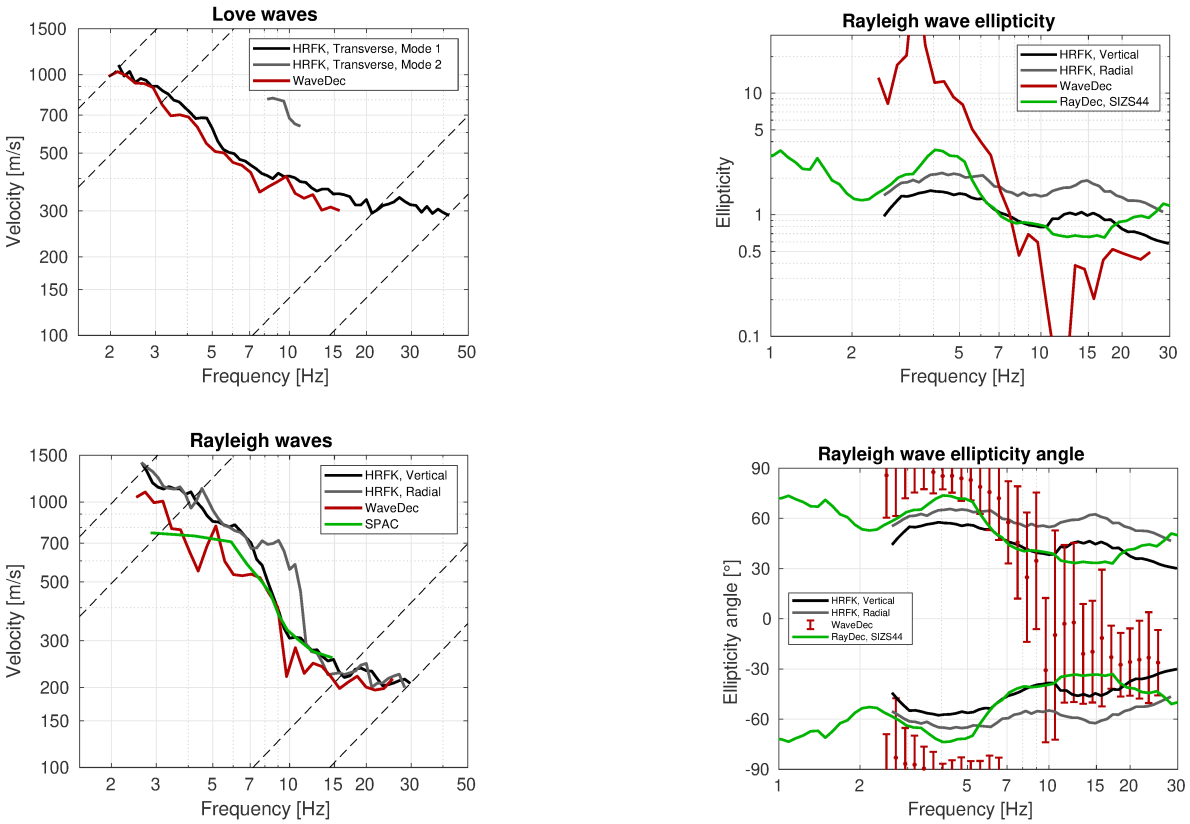

Figure 9: Overview of the Love and Rayleigh wave dispersion curves as well as the ellipticity and ellipticity angle curves for both arrays. The dashed lines indicate the theoretical resolution limits of the array. The RayDec ellipticity curve corresponds to station SIZS44.

4 Data inversion

4.1 Inversion targets

Two different inversion targets are defined. For target 1, we use the Love and Rayleigh wave dispersion curves together with the Rayleigh wave ellipticity angle. For target 2, only the Rayleigh wave dispersion and ellipticity angle curves are used.
The curve picked for HRFK on the transverse component was assumed as the fundamental mode Love wave dispersion curve. For the Rayleigh wave dispersion curve, the picked HRFK curve for the vertical component was used.
For both targets 1 and 2, parts of the WaveDec and the RayDec curve were used as ellipticity angle information. The WaveDec curve between 3.12 and 3.45 Hz, which is retrograde, fixes the ellipticity angle below the fundamental peak. The prograde WaveDec curve between 4.20 and 4.42 Hz fixes the angle above the peak. The peak frequency is left free in between. Furthermore, the RayDec curve is used between 5.12 and 7.62 Hz, assuming prograde particle motion, to further fix the ellipticity angle. The details of the inversion targets are indicated in Table 1 and the corresponding curves are shown in Fig. 10.

4.2 Inversion parameterization

Six different parameterizations have been used in total. The first five had free values of the depths and velocities of the different layers, ranging from four to eight layers (including the half-space). The last parameterization had fixed layer depths and consisted of 20 layers in total. The main interface depths resulting from the 8-layer inversion were used in the fixed-layer approach. The P-wave velocities were allowed to vary up to 5000 m/s. The S-wave velocities were allowed to range from 30 to 3500 m/s. The deepest layers were parameterized to reach a depth of 200 m maximum. The density was fixed to 2 300 kg/m^3 for the lowest layer, to 1 900 kg/m^3 for the superficial layer (or the first three layers in the fixed-layer case) and to 2 100 kg/m^3 for all other layers. No low-velocity zones were allowed.

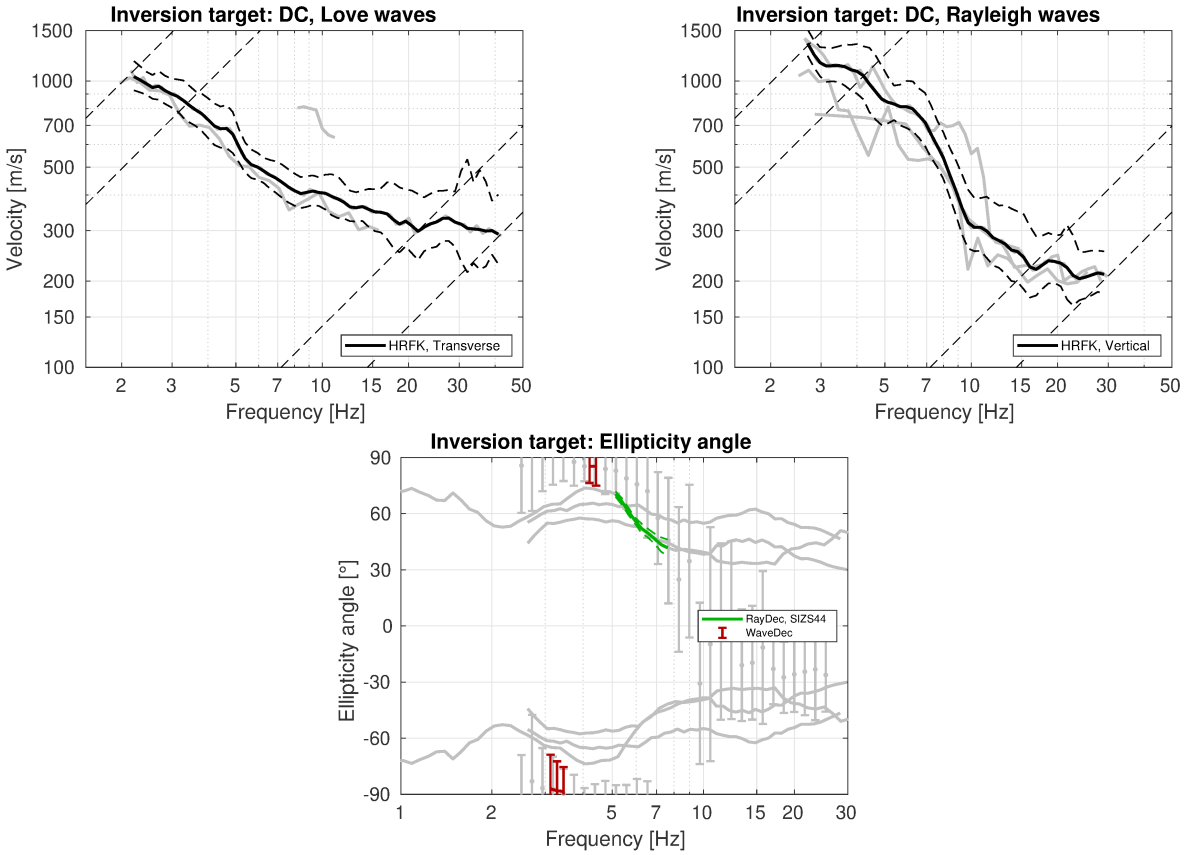

Figure 10: Overview of the dispersion (top) and ellipticity angle (bottom) curves used as targets for the different inversions.

Table 1: List of the different data curves used as target in the different inversions. For target 1, all listed curves where used. For target 2, the Love wave dispersion curve was not used.

Method	Wave type	Mode	Curve type	Frequency range [Hz]
HRFK (T)	Love	fundamental	dispersion	2.21 - 41.0
HRFK (V)	Rayleigh	fundamental	dispersion	2.69 - 29.0
WaveDec	Rayleigh	fundamental	ellipticity angle	3.12 - 3.45
WaveDec	Rayleigh	fundamental	ellipticity angle	4.20 - 4.42
RayDec (SIZS44)	Rayleigh	fundamental	ellipticity angle	5.12 - 7.62

4.3 Inversion results

We performed six inversions with different parameterizations for each of the two targets. In Table 2, the obtained minimum misfit values for these inversions are shown. Each inversion run produced around 150 000 total models in order to assure a good convergence of the solution, except for the 4-layer inversion, where 100 000 generated models were sufficient. The results of the inversions SIZS4l1 to SIZSfix1, using target 1, are shown in Figs 11 - 16 and the results for inversions SIZS4l2 to SIZSfix2, using target 2, in Figs 17 - 22.

The different inversions for the respective targets yield similar misfit values and fit the data in a comparable way. The 4-layer inversions yield slightly higher misfit values than the 6-, 7- and 8-layer inversions. Using the fixed-depth approach, the minimum misfit was also higher, probably because the interface depths were fixed at non-optimum depths. For the inversions with target 1, the misfits are significantly higher than for target 2, because it Love and Rayleigh wave dispersion curves had to be fitted at the same time.

Table 2: List of inversions

Inversion	Number of layers	Number of models	Minimum misfit
SIZS4l1	4	100 065	0.860
SIZS5l1	5	150 024	0.841
SIZS6l1	6	149 998	0.846
SIZS7l1	7	150 091	0.852
SIZS8l1	8	150 039	0.863
SIZSfix1	20	150 020	0.959
SIZS4l2	4	100 031	0.662
SIZS5l2	5	150 006	0.637
SIZS6l2	6	150 018	0.622
SIZS7l2	7	150 074	0.635
SIZS8l2	8	150 061	0.643
SIZSfix2	20	150 033	0.682

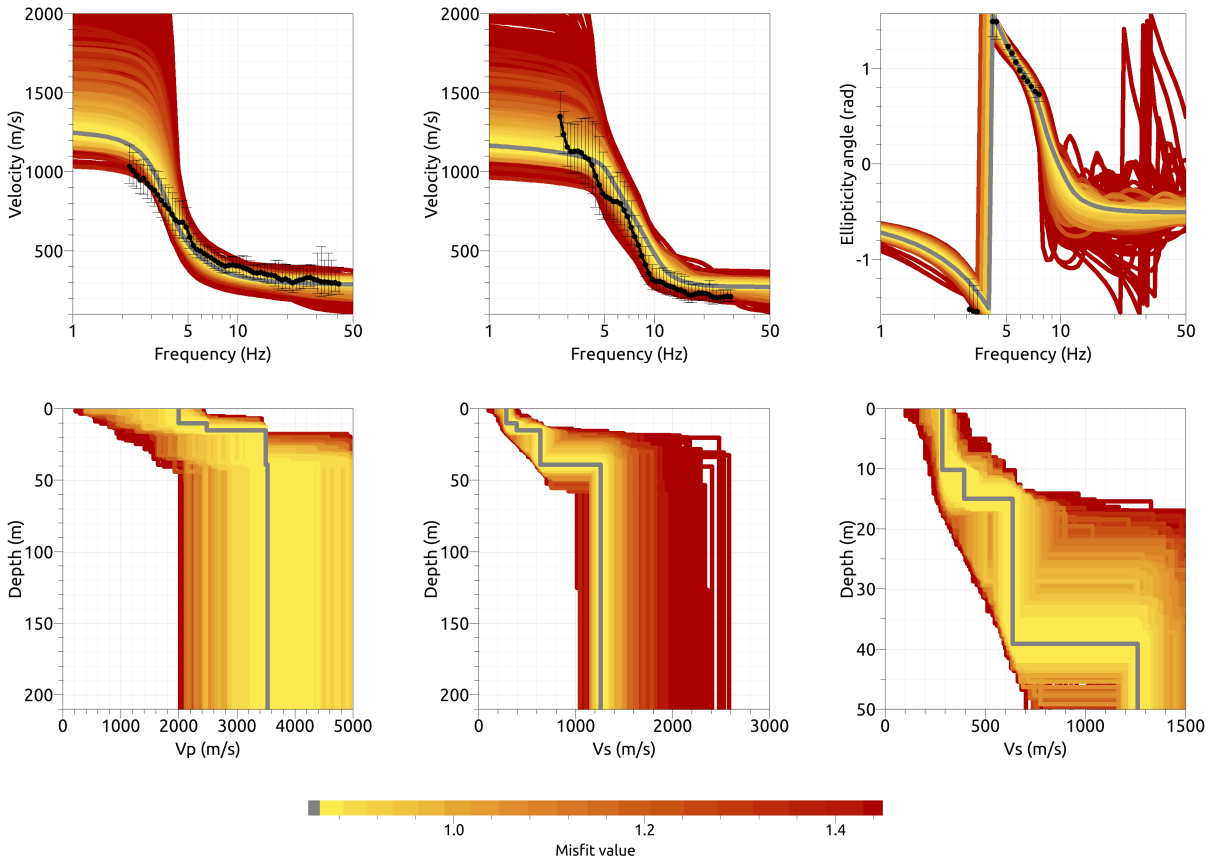

Figure 11: Inversion SIZS4l1. Top line: Dispersion curves for Love waves (left) and Rayleigh waves (center) and Rayleigh wave ellipticity angle (right) of the respective fundamental modes. Bottom line: P-wave velocity profiles (left), S-wave velocity profiles (center and zoom on the right). The black dots indicate the data points used for the inversion, the gray line indicates the best-fitting model.

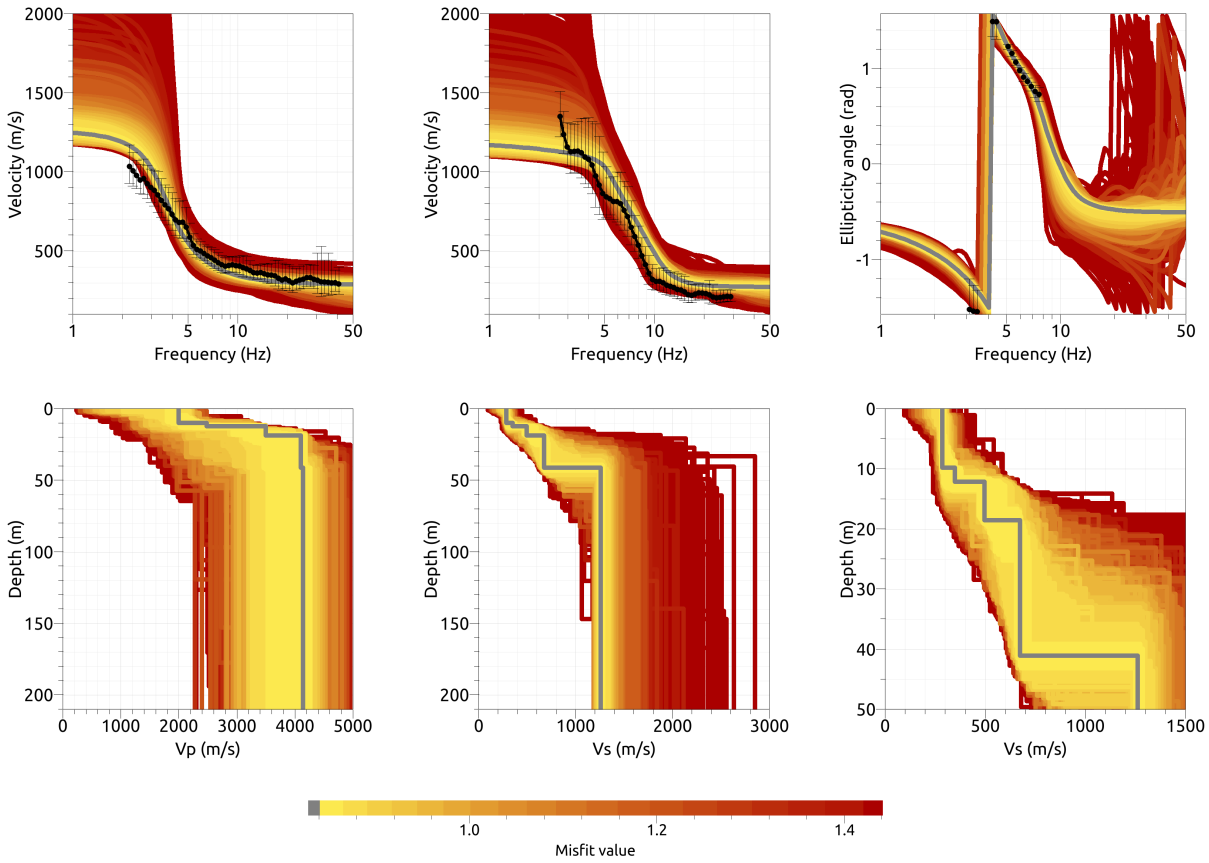

Figure 12: Inversion SIZS5l1. Top line: Dispersion curves for Love waves (left) and Rayleigh waves (center) and Rayleigh wave ellipticity angle (right) of the respective fundamental modes. Bottom line: P-wave velocity profiles (left), S-wave velocity profiles (center and zoom on the right). The black dots indicate the data points used for the inversion, the gray line indicates the best-fitting model.

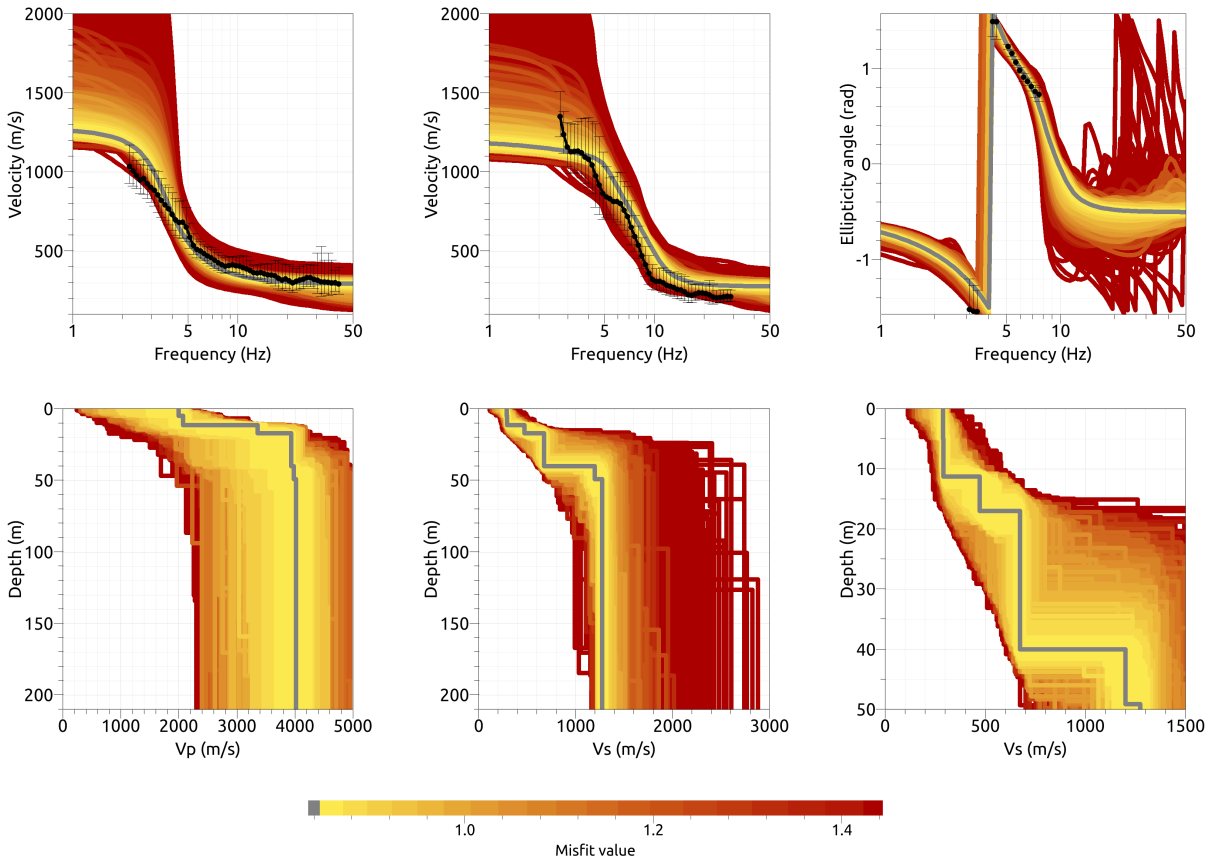

Figure 13: Inversion SIZS6l1. Top line: Dispersion curves for Love waves (left) and Rayleigh waves (center) and Rayleigh wave ellipticity angle (right) of the respective fundamental modes. Bottom line: P-wave velocity profiles (left), S-wave velocity profiles (center and zoom on the right). The black dots indicate the data points used for the inversion, the gray line indicates the best-fitting model.

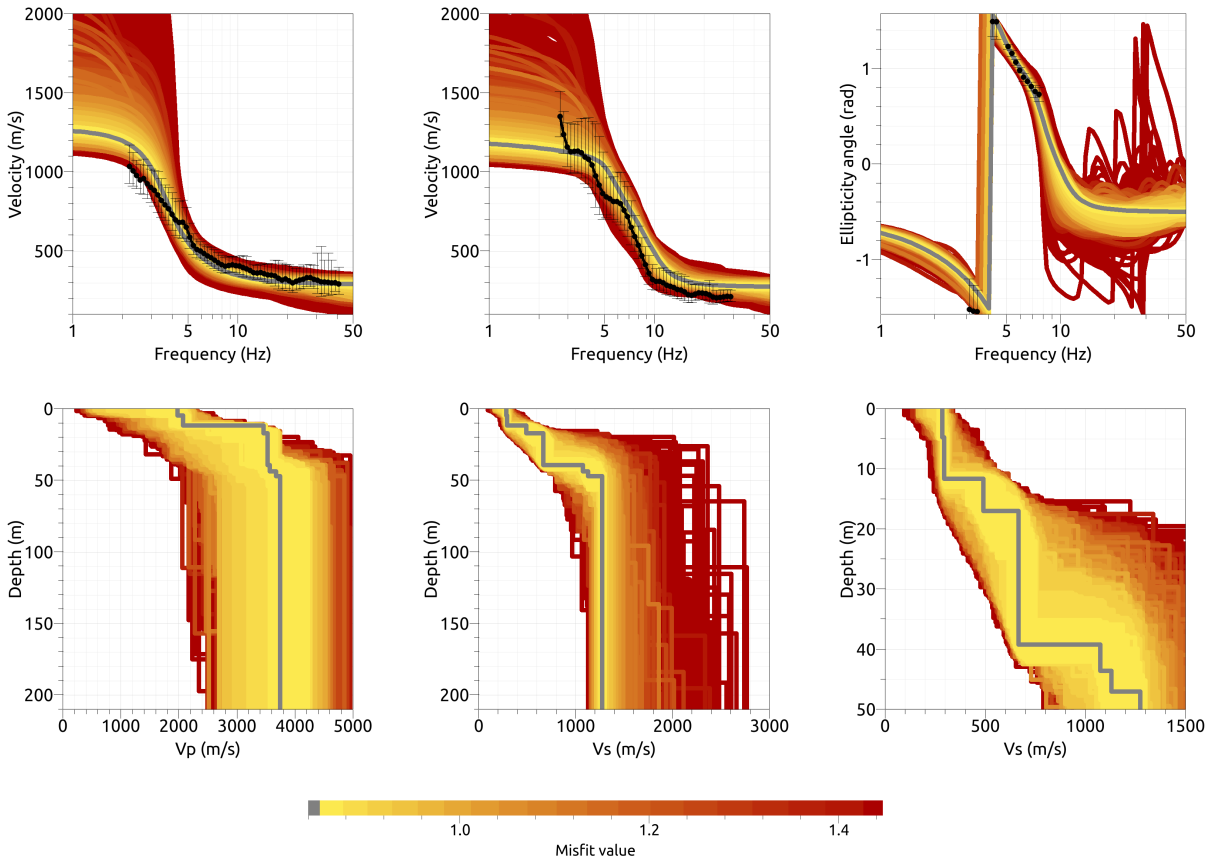

Figure 14: Inversion SIZS7l1. Top line: Dispersion curves for Love waves (left) and Rayleigh waves (center) and Rayleigh wave ellipticity angle (right) of the respective fundamental modes. Bottom line: P-wave velocity profiles (left), S-wave velocity profiles (center and zoom on the right). The black dots indicate the data points used for the inversion, the gray line indicates the best-fitting model.

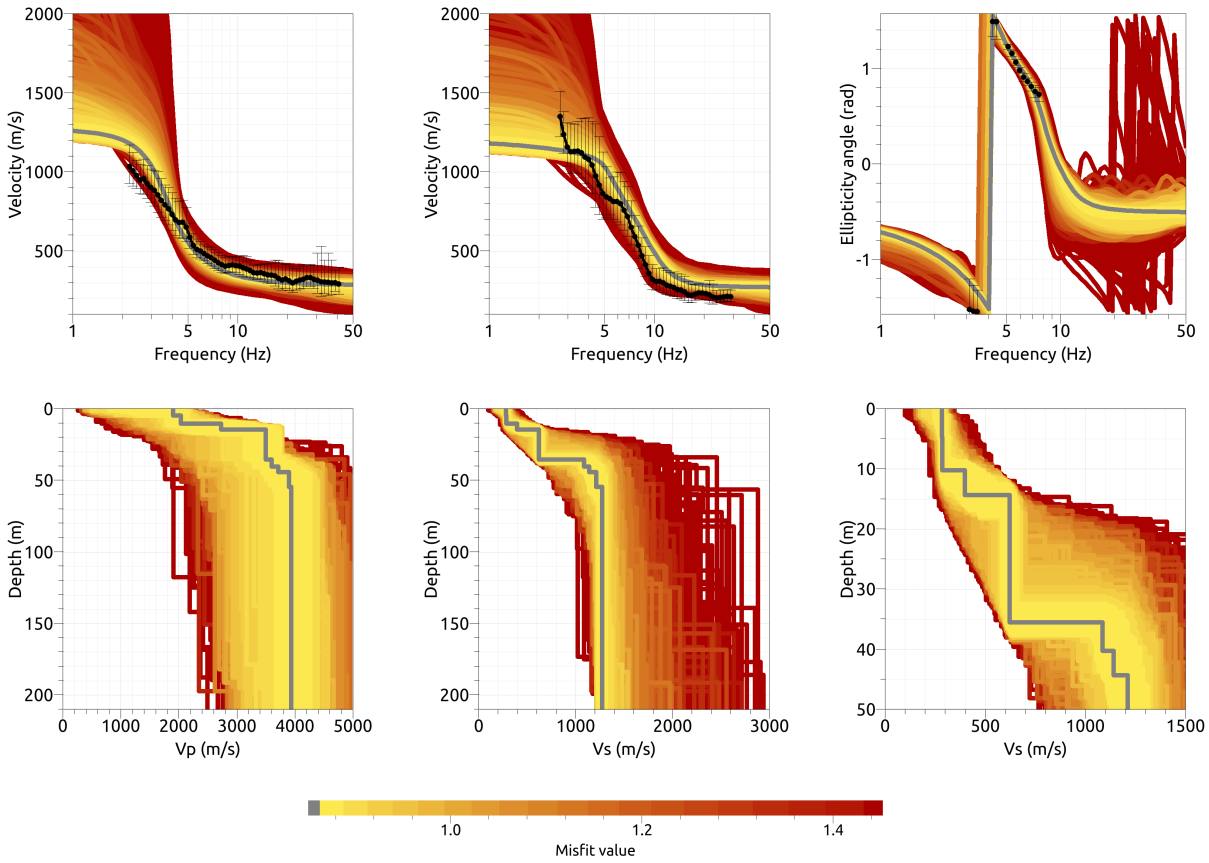

Figure 15: Inversion SIZS8l1. Top line: Dispersion curves for Love waves (left) and Rayleigh waves (center) and Rayleigh wave ellipticity angle (right) of the respective fundamental modes. Bottom line: P-wave velocity profiles (left), S-wave velocity profiles (center and zoom on the right). The black dots indicate the data points used for the inversion, the gray line indicates the best-fitting model.

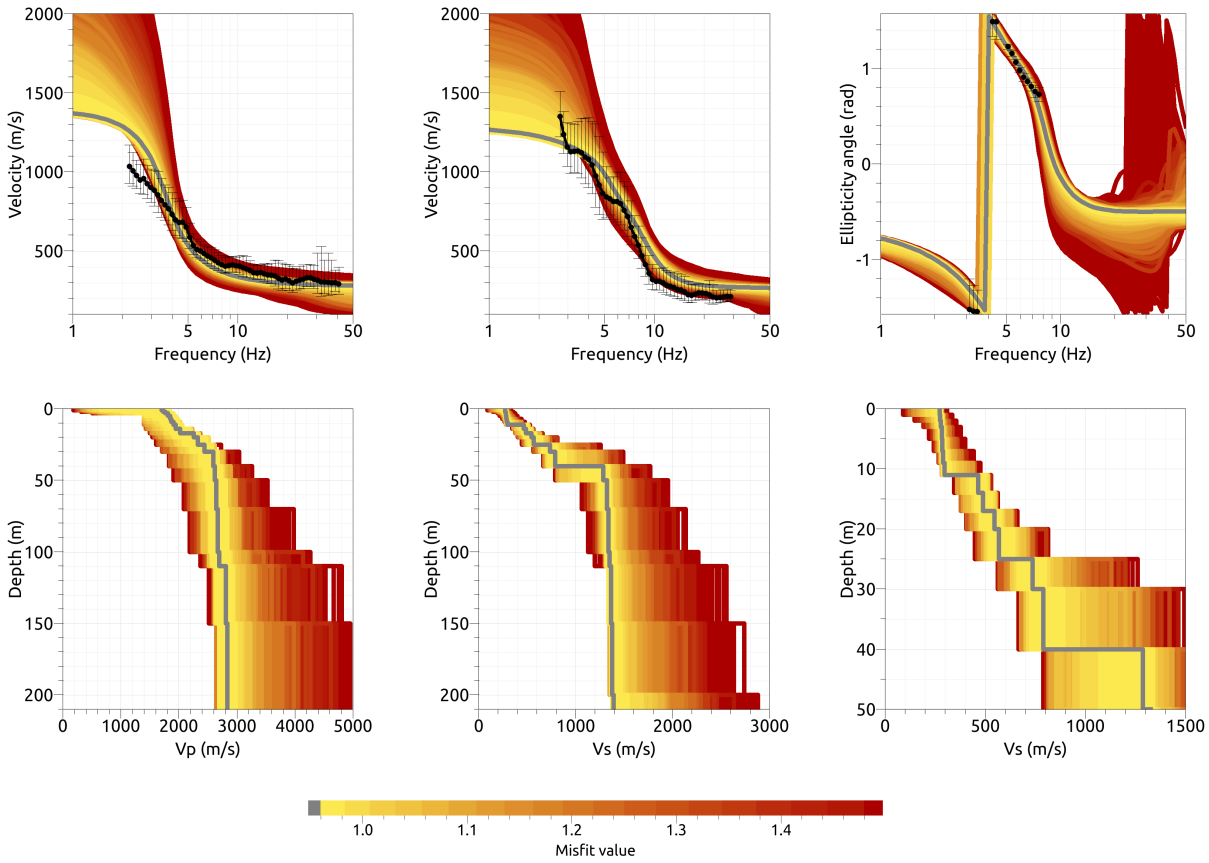

Figure 16: Inversion SIZSfix1. Top line: Dispersion curves for Love waves (left) and Rayleigh waves (center) and Rayleigh wave ellipticity angle (right) of the respective fundamental modes. Bottom line: P-wave velocity profiles (left), S-wave velocity profiles (center and zoom on the right). The black dots indicate the data points used for the inversion, the gray line indicates the best-fitting model.

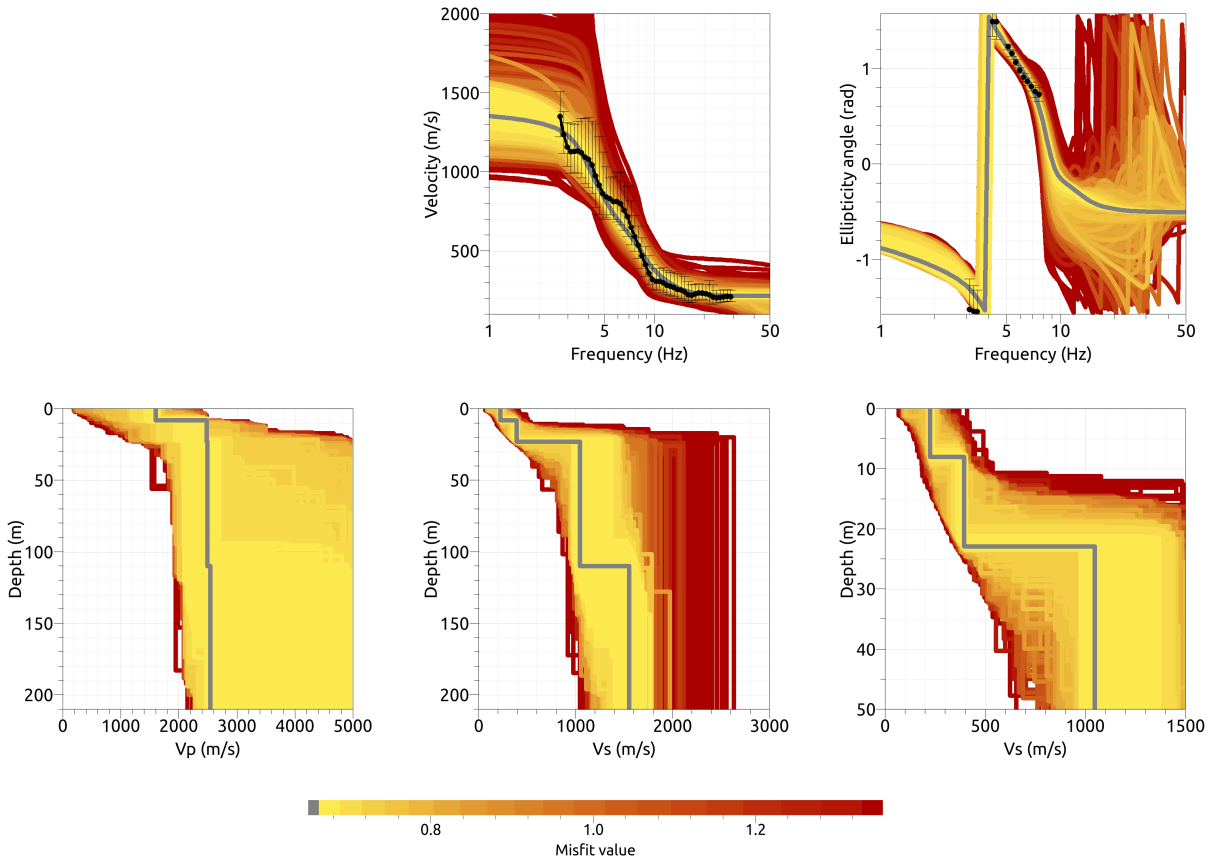

Figure 17: Inversion SIZS4l2. Top line: Rayleigh wave dispersion curves (center) and Rayleigh wave ellipticity angle (right) of the fundamental mode. Bottom line: P-wave velocity profiles (left), S-wave velocity profiles (center and zoom on the right). The black dots indicate the data points used for the inversion, the gray line indicates the best-fitting model.

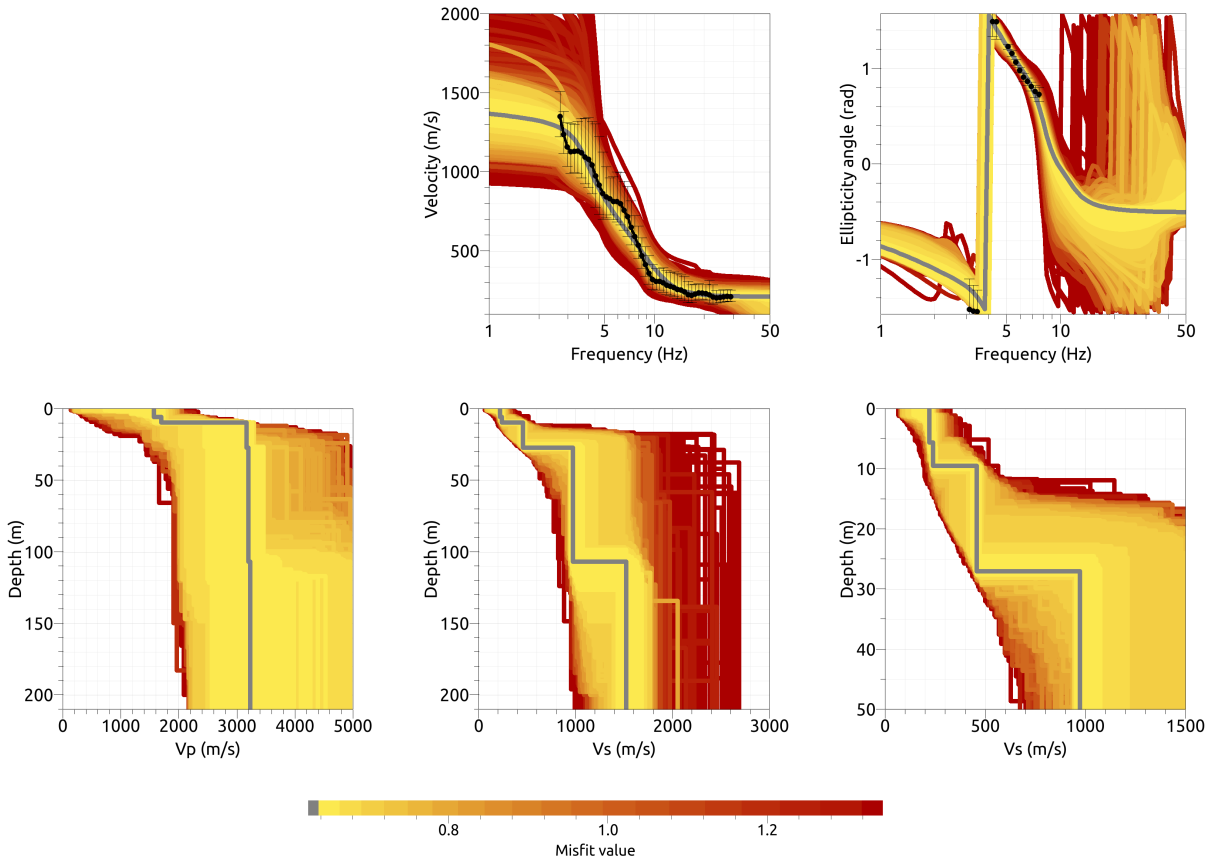

Figure 18: Inversion SIZS5l2. Top line: Rayleigh wave dispersion curves (center) and Rayleigh wave ellipticity angle (right) of the fundamental mode. Bottom line: P-wave velocity profiles (left), S-wave velocity profiles (center and zoom on the right). The black dots indicate the data points used for the inversion, the gray line indicates the best-fitting model.

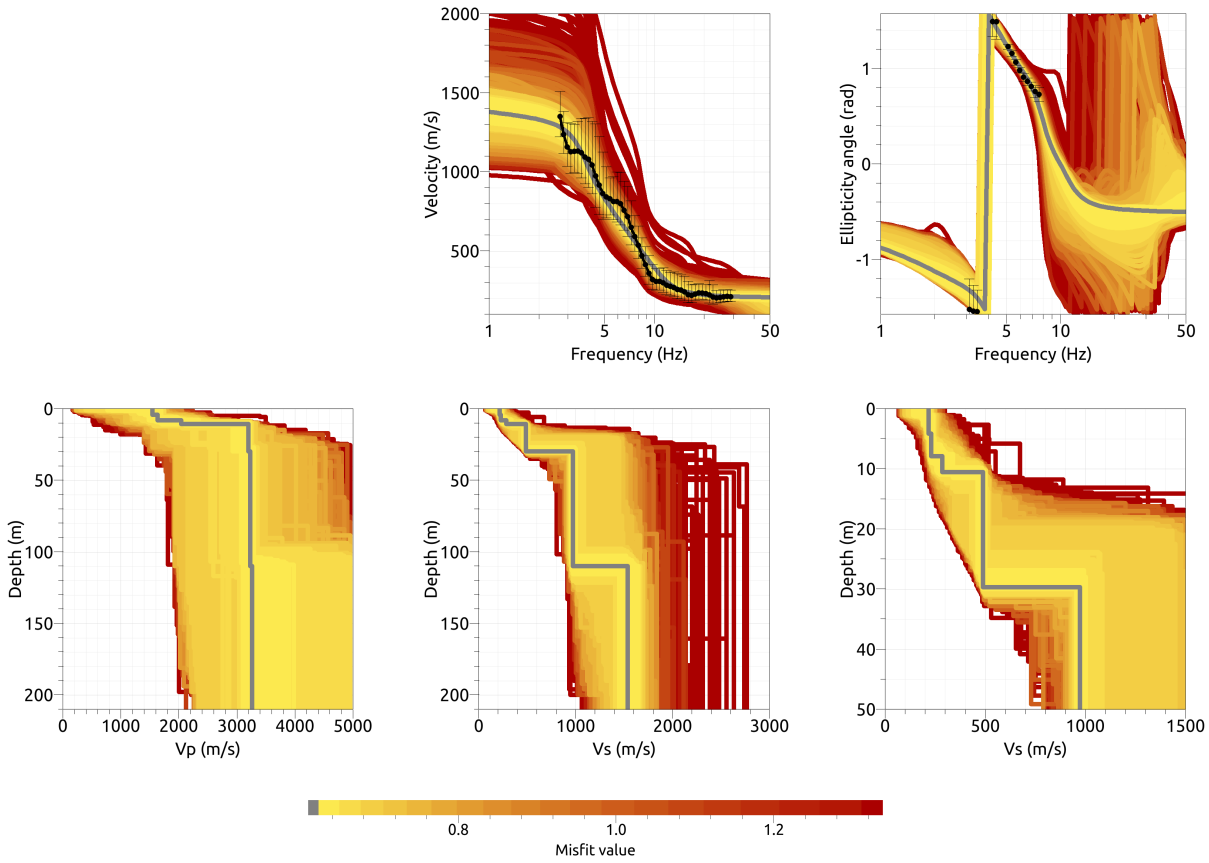

Figure 19: Inversion SIZS6l2. Top line: Rayleigh wave dispersion curves (center) and Rayleigh wave ellipticity angle (right) of the fundamental mode. Bottom line: P-wave velocity profiles (left), S-wave velocity profiles (center and zoom on the right). The black dots indicate the data points used for the inversion, the gray line indicates the best-fitting model.

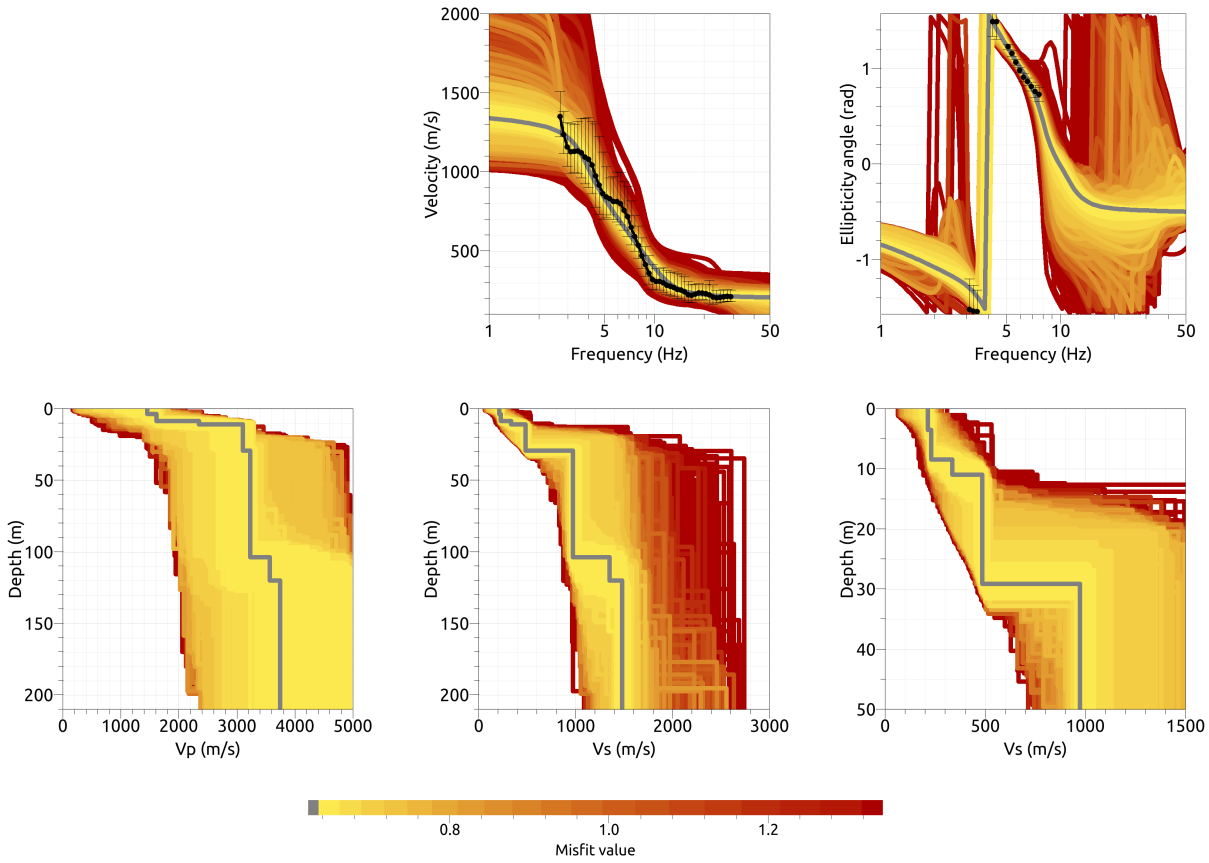

Figure 20: Inversion SIZS7l2. Top line: Rayleigh wave dispersion curves (center) and Rayleigh wave ellipticity angle (right) of the fundamental mode. Bottom line: P-wave velocity profiles (left), S-wave velocity profiles (center and zoom on the right). The black dots indicate the data points used for the inversion, the gray line indicates the best-fitting model.

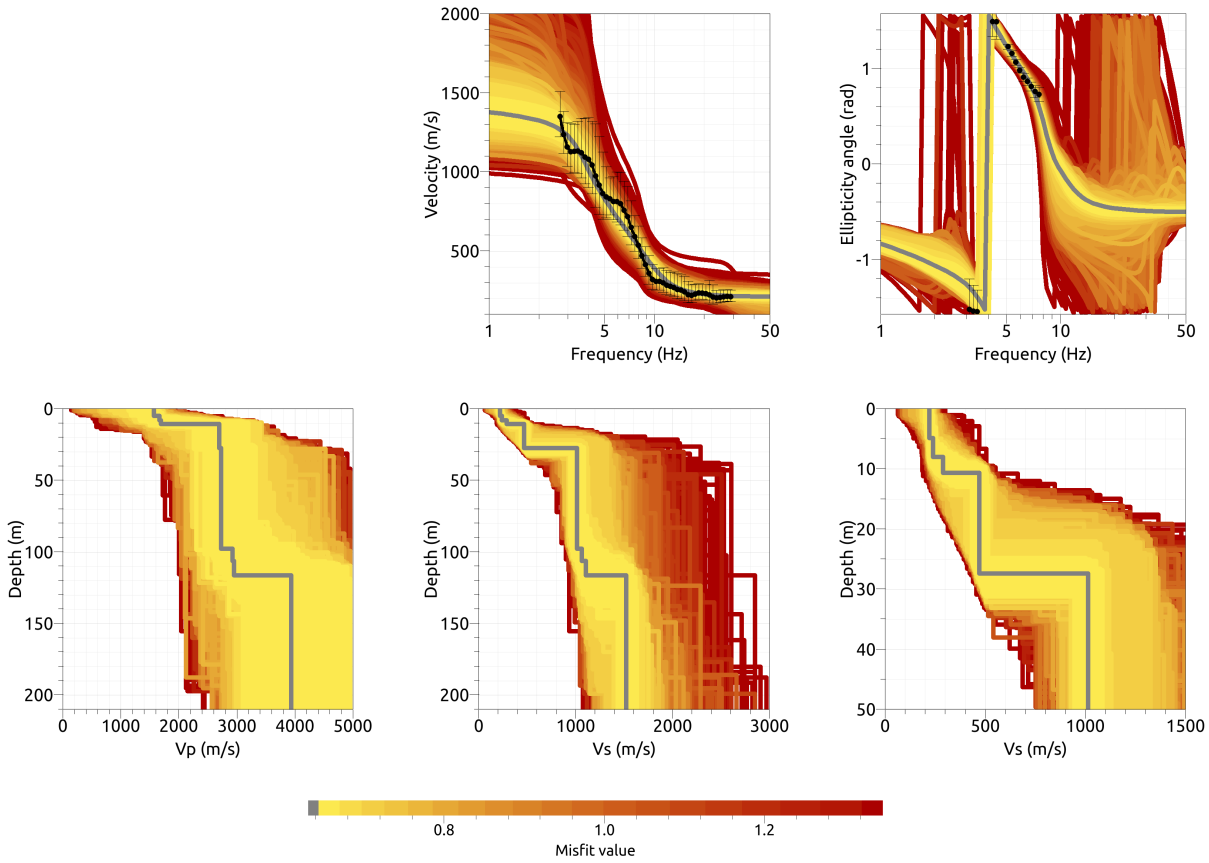

Figure 21: Inversion SIZS8l2. Top line: Rayleigh wave dispersion curves (center) and Rayleigh wave ellipticity angle (right) of the fundamental mode. Bottom line: P-wave velocity profiles (left), S-wave velocity profiles (center and zoom on the right). The black dots indicate the data points used for the inversion, the gray line indicates the best-fitting model.

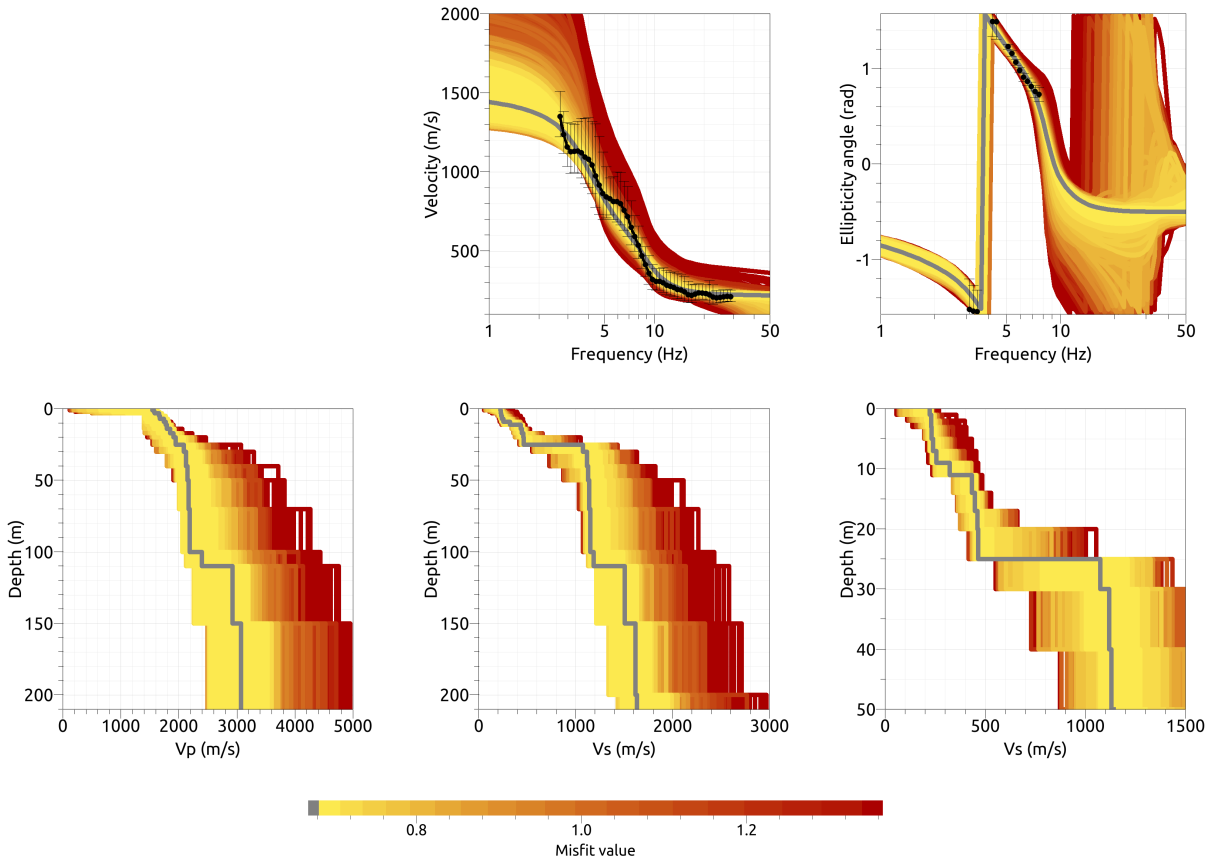

Figure 22: Inversion SIZSfix2. Top line: Rayleigh wave dispersion curves (center) and Rayleigh wave ellipticity angle (right) of the fundamental mode. Bottom line: P-wave velocity profiles (left), S-wave velocity profiles (center and zoom on the right). The black dots indicate the data points used for the inversion, the gray line indicates the best-fitting model.

4.4 Overview of the inversion result

The S-wave velocity profiles of the best-fitting models of all inversions are shown in Fig. 23. The models of the respective targets show similar main features, but differ for the different targets. The models for target 1 (Rayleigh and Love wave curves) have shear-wave velocities of about 285 m/s from the surface to about 10 m of depth, where the velocity increases in several steps to values between 620 and 672 m/s at depths between 39 and 41 m, where a strong velocity contrast is found and the velocity increases to over 1250 m/s. For models with more layers, especially the fixed-depth approach, the transitions are smoother with more steps.
For the inversions with target 2 (using only Rayleigh wave curves), the shear-wave velocity at the surface is smaller, with values between 215 and 227 m/s. A strong velocity increase occurs between 8 and 11 m depth, where the velocity increases to values between 455 and 490 m/s. Another strong contrast is found between 23 and 30 m of depth, where the velocity increases to values between 970 and 1100 m/s. These models show another increase to velocities of around 1500 m/s at depths between 103 and 120 m.
The V_{S30} values for the inversions using target 1 range from 415.8 to 427.8 m/s (average value $422.9 \pm 4.5\, m/s$). For target 2, the V_{S30} values range from 357.3 to 377.2 m/s (average value $366.0 \pm 8.3\, m/s$). In both cases, this corresponds to soil class B in EC8 and C in SIA261.

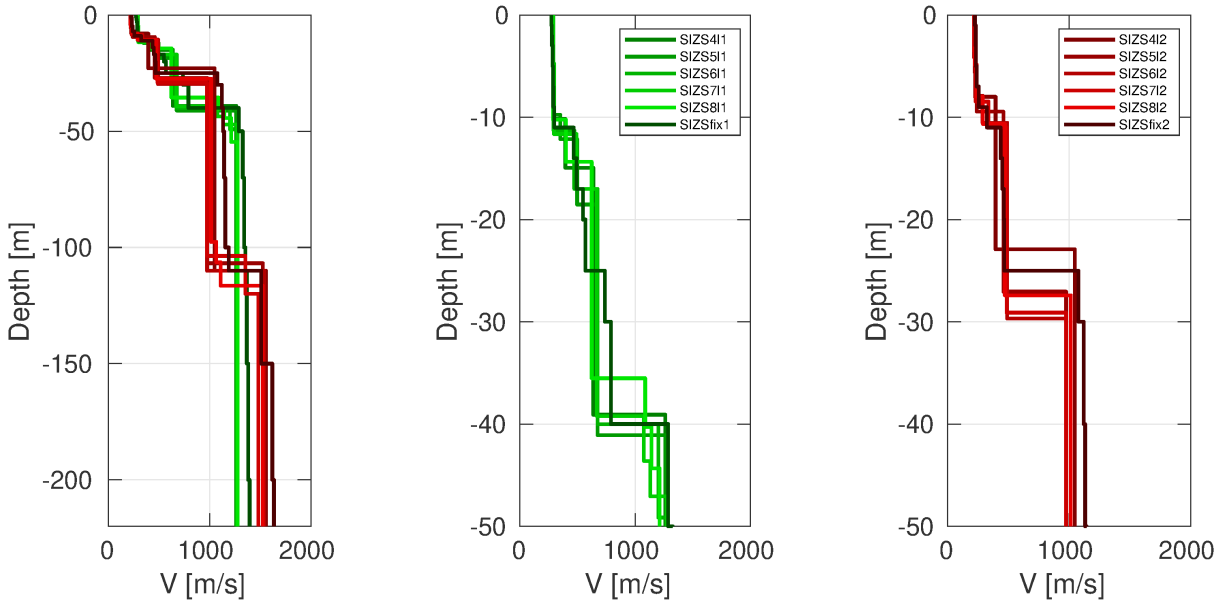

Figure 23: Overview of shear-wave velocity profiles of the best-fitting models of all inversions (left) and a zoom on the shallow part for the inversions using target 1 (center) and target 2 (right).

4.5 Amplification function

In Fig. 24, the theoretical amplification function for the best models resulting from the inversions is compared with the empirical amplification of station SIZS, based on 25 events so far. The empirical amplification shows a first peak at around 1.4 Hz, followed by a trough at about 2.3 Hz and a second, more pronounced peak at around 4.0 Hz. Above, the empirical amplification decreases and we even observe deamplification around 20 Hz. In the inversions, we did not use the ellipticity peak around 1 Hz because it was rather wide and not very clear. Including this peak in the inversion might have resulted in models with an amplification peak around this frequency. In any case, both inversion results, using target 1 and target 2, show a good fit of the resulting modeled amplification with the empirical one around 4 Hz. The modeled amplification for target 1 shows an amplification peak at 3.95 Hz, in better agreement with the empirical amplification than the 4.5 Hz peak modeled for target 2. The peaks modeled for higher frequencies do not match the observed amplification curve.
Based on the amplification modeling and because it also includes the measured Love wave dispersion curve to constrain the structure, we choose the results of the inversion with target 1 as representative results for the site.

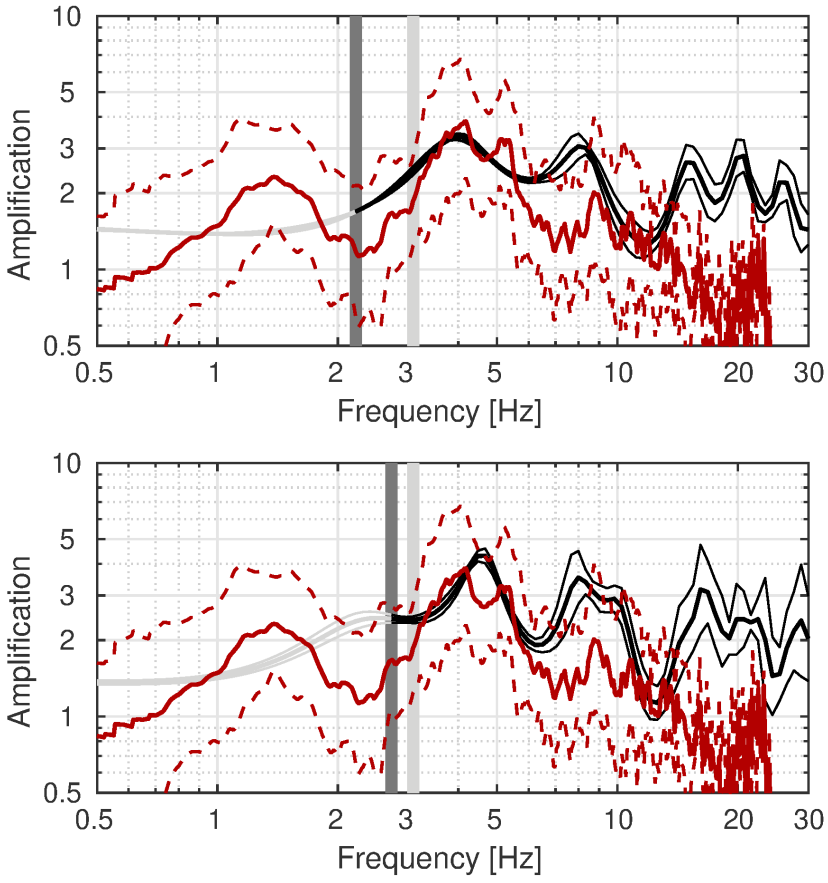

Figure 24: Comparison between the modeled amplification for the final set of best models of the different inversions (in grey to black, with standard deviation) and the empirical amplification measured at station SIZS (red, with standard deviation) for target 1 (top) and target 2 (bottom). The vertical light and dark grey bars correspond to the lowest frequency of the ellipticity and dispersion curves used for the inversion, respectively.

4.6 Quarter-wavelength representation

The quarter-wavelength velocity approach (Joyner et al., 1981) provides, for a given frequency, the average velocity at a depth corresponding to 1/4 of the wavelength of interest. It is useful to identify the frequency limits of the experimental data (the minimum frequency of the dispersion curve used in the inversion is 2.21 Hz for target 1 and 2.69 Hz for target 2, the minimum frequency used for the ellipticity inversion 3.12 Hz). The results using this proxy show that the dispersion curves constrain the profiles down to about 73 m for target 1 and 42 m for target 2 (Fig. 25). Moreover, the quarter wavelength impedance-contrast introduced by Poggi et al. (2012) is also displayed in the figure. It corresponds to the ratio between two quarter-wavelength average velocities, respectively from the top and the bottom part of the velocity profile, at a given frequency (Poggi et al., 2012). This curve shows a strong contrast at the fundamental frequency of the site.

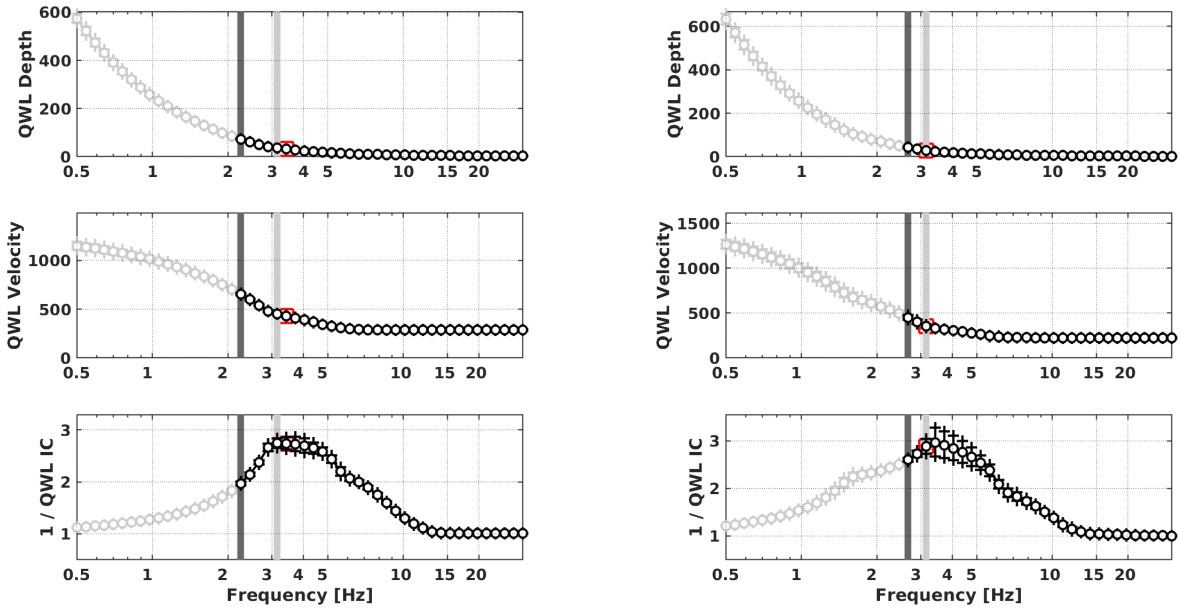

Figure 25: Quarter wavelength representation of the velocity profile for the best models of the inversions (top: depth, center: velocity, bottom: inverse of the impedance contrast) for the resulting models of target 1 (left) and target 2 (right). The black curves are constrained by the dispersion curves, the light grey curves are not constrained by the data. The red square corresponds to V_{S30}.

5 Conclusion

We performed a passive array measurement to characterize the soil underneath station SIZS in Ilanz/Glion (GR). According to the geological atlas, the station is located on moraine.
The dispersion curves for Love and Rayleigh waves could be measured over a wide frequency range, from around 2.1 to 42 Hz for Love waves and from 2.6 to 29.7 Hz for Rayleigh waves. In the H/V and ellipticity curves, a broad peak is found around 1 Hz and a more pronounced peak at around 4 Hz, which, according to the WaveDec measurements, corresponds to a singularity where the particle motion changes the sense of rotation.
Two different joint inversions wer performed, using different parameterizations in each case. The first target consisted of the measured Love and Rayleigh wave dispersion curves and the Rayleigh wave ellipticity angle. The second target did not include the Love wave dispersion curve. Both inversions were able to fit the data in a good way. We choose the inversions with the first target as representative for the site because they are based on more measured data. These models show a structure with interfaces at around 10 m, and 40 m, with a V_{S30} of about 423 m/s, corresponding to soil class B in EC8 and C in SIA261.

Acknowledgements

The authors thank David Farsky and Simon Rouwendaal for their help during the array measurements.

References

Aki, K. (1957). Space and time spectra of stationary stochastic waves, with special reference to microtremors. *Bull. Earthquake Res. Inst. Tokyo Univ.*, 35:415–456.

Bettig, B., Bard, P.-Y., Scherbaum, F., Riepl, J., Cotton, F., Cornou, C., and Hatzfeld, D. (2001). Analysis of dense array noise measurements using the modified spatial auto-correlation method (SPAC): application to the Grenoble area. *Boll. Geof. Teor. Appl.*, 42:281–304.

Burjánek, J., Gassner-Stamm, G., Poggi, V., Moore, J. R., and Fäh, D. (2010). Ambient vibration analysis of an unstable mountain slope. *Geophys. J. Int.*, 180:820–828.

Burjánek, J., Moore, J. R., Molina, F. X. Y., and Fäh, D. (2012). Instrumental evidence of normal mode rock slope vibration. *Geophys. J. Int.*, 188:559–569.

Fäh, D., Wathelet, M., Kristekova, M., Havenith, H., Endrun, B., Stamm, G., Poggi, V., Burjanek, J., and Cornou, C. (2009). Using ellipticity information for site characterisation. NERIES deliverable JRA4 D4, available at http://www.neries-eu.org.

Hobiger, M., Bard, P.-Y., Cornou, C., and Le Bihan, N. (2009). Single station determination of Rayleigh wave ellipticity by using the random decrement technique (RayDec). *Geophys. Res. Lett.*, 36.

Joyner, W. B., Warrick, R. E., and Fumal, T. E. (1981). The effect of Quaternary alluvium on strong ground motion in the Coyote Lake, California, earthquake of 1979. *Bull. Seismol. Soc. Am.*, 71(4):1333–1349.

Maranò, S., Reller, C., Loeliger, H.-A., and Fäh, D. (2012). Seismic waves estimation and wavefield decomposition: Application to ambient vibrations. *Geophys. J. Int.*, 191:175–188.

Poggi, V., Edwards, B., and Fäh, D. (2012). Characterizing the Vertical-to-Horizontal ratio of ground motion at soft-sediment sites. *Bull. Seismol. Soc. Am.*, 102(6):2741–2756.

Poggi, V. and Fäh, D. (2010). Estimating Rayleigh wave particle motion from three-component array analysis of ambient vibrations. *Geophys. J. Int.*, 180:251–267.

Wathelet, M., Jongmans, D., and Ohrnberger, M. (2005). Direct inversion of spatial autocorrelation curves with the neighborhood algorithm. *Bull. Seismol. Soc. Am.*, 95:1787–1800.